



Letter

# The synergistic effect of neutron irradiation on the tensile properties of Fe-0.74 wt.% Ni alloy: A combined study of machine-learning and molecular dynamics

Chang-Chun He <sup>a,b</sup>, Fen Ren <sup>a</sup>, Xiao-Bao Yang <sup>b</sup>, Guiyi Wu <sup>a,\*</sup>, Shuyan Zhang <sup>a</sup><sup>a</sup> Centre of Excellence for Advanced Materials, Dongguan, Guangdong, 523808, China<sup>b</sup> Department of Physics, South China University of Technology, Guangzhou, 510641, China

## ARTICLE INFO

Communicated By Lilia Woods

## Keywords:

Molecular dynamics  
Machine-learning potential  
Irradiation defects  
Synergistic effects  
Stress-strain

## ABSTRACT

The aim of this study is to elucidate the mechanisms of irradiation damage to reactor pressure vessel (RPV) steel using a machine learning algorithms and high-throughput calculations. Various Fe-Ni alloy structures were generated based on structural enumeration for high-throughput first-principles calculations, with the Fe-Ni interatomic potential trained using a Gaussian approximation function. Simulations were conducted using LAMMPS software to investigate the effects of neutron irradiation on the tensile properties of Fe-0.74 wt.% Ni alloy, utilizing the well-established Fe-Ni interatomic potential. The irradiation dose significantly impacts defects in the Fe-Ni alloy. Synergistic effects of alloy solute element content and temperature with irradiation defects reveal that defect numbers at irradiation points increase linearly with MD-dpa and PKA energy. During irradiation, Ni atoms diffuse via the exchange with vacancy, synergizing with other Ni elements. Notably, Ni content inversely affects yield stress, resulting in lower yield stress in irradiated materials compared to pre-irradiation levels. While temperature inversely affects yield stress, its synergistic effect with defects increases yield stresses post-irradiation, known as irradiation hardening. Post-irradiation, the yield strain increases, and a flat plateau stress region is observed in Fe-Ni alloys. Ni atoms act as a buffer during the stretching process, contributing to a relatively gentle slope stress region despite increasing stress. The distribution of Ni atoms significantly influences the stress-strain curve, in which the aggregated Ni atoms decrease yield strength, whereas uniform distribution increases it, highlighting Ni atoms as buffering role during stretching process. These simulations yield valuable insights for exploring scalability and enhancing the development of irradiation hardening and embrittlement models.

## 1. Introduction

The service environment of nuclear reactor pressure vessel (RPV) steel is extremely harsh, subjecting the material to high temperatures, pressures, intense corrosion, and radiation over extended periods. These conditions lead to profound changes in microstructure and mechanical properties, significantly reducing the service life of nuclear materials [1, 2]. Looking forward to future Generation IV fission and fusion energy systems, several key radiation-induced degradation effects affect structural materials, including low temperature radiation hardening and embrittlement, radiation-induced and modified solute segregation, phase stability, irradiation creep, ineffective swelling, and high temperature helium embrittlement [3]. Neutron irradiation induces the

aggregation and evolution of supersaturated point defects in RPV steels, resulting in microscopic products such as dislocation rings, solute clusters, voids, and laminated tetrahedra. These defects contribute to phenomena like irradiation swelling [4], hardening [5-7], embrittlement [8-10], segregation [11,12], and helium bubble formation [13,14]. High-energy particle collisions from irradiation create defects that hinder dislocation slip, profoundly impacting the mechanical properties of nuclear structural materials by increasing yield and flow stresses while reducing ductility. Atomic-scale computer simulations [15] provide insights into how irradiation dose, solute element content, strain rate, and temperature influence these cascade effects [16,17]. For commonly used RPV material SA508-3 steel, irradiation defects notably affect tensile properties. Recent research has focused on irradiation

\* Corresponding author.

E-mail address: [guiyi.wu@ceamat.com](mailto:guiyi.wu@ceamat.com) (G. Wu).

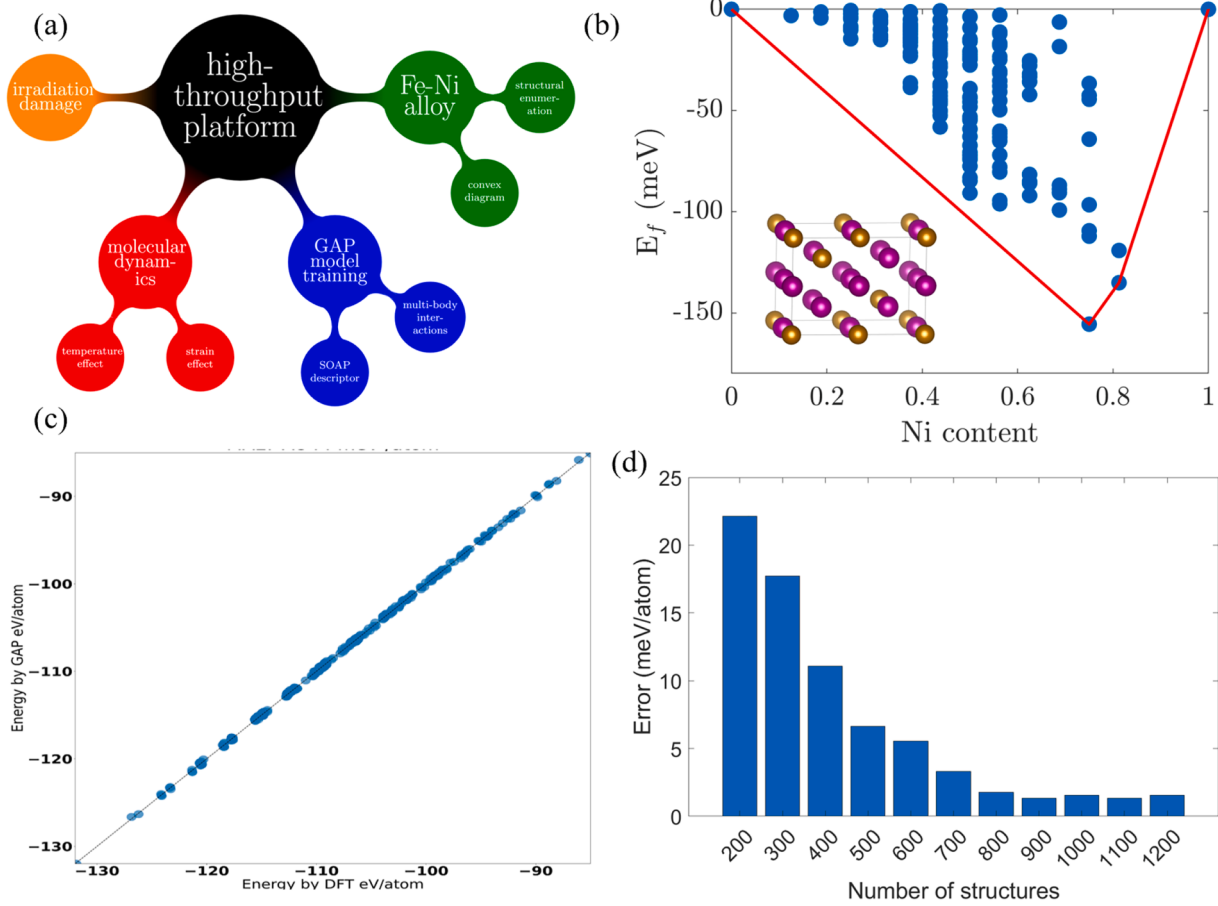


**Fig. 1.** (a) high-throughput calculations and machine learning potential construction diagram. (b) The formation energy of Fe-Ni alloy structures as a function of the concentration of Ni element in the  $2 \times 2 \times 1$  supercell, and the red line show the structures at the convexhull, where the ground state alloy structures are plotted in the left lower corner. (c) The linear relationship of the total energy predicted by GAP model and DFT. (d) The convergence testing of multiple Fe-Ni structures for GAP model training.

damage in pure iron, the aggregation and evolution of irradiation point defects [11,12,17], dislocation behavior [18–20], dislocation ring formation [21,22], and the interaction between grain boundaries and irradiation defects [23]. However, studies on the complex synergistic effects of solute elements, irradiation dose, and temperature during irradiation and tension in steel remain limited. Understanding how tensile properties change at the atomic scale post-irradiation, compared to their mesoscopic and macroscopic counterparts derived from finite element modeling and experimental tests, presents challenges in data transfer and evolution across scales in multi-scale simulation processes.

It has been established that solutes such as Cu, Ni, Mn, and Si significantly influence the irradiation embrittlement of reactor pressure vessel (RPV) steels, each diffusing within the steel through distinct mechanisms. Ni, Cu, and Si primarily diffuse via vacancy mechanisms, whereas Mn predominantly uses interstitial mechanisms. Over the past 25 years, a series of advanced mechanistic models for radiation embrittlement have been developed, offering comprehensive insights into the intricate and synergistic effects involving solutes (Cu, Ni, P), temperature, dose, and irradiation flux [8,10,24,25]. Studies by Vincent et al. [26,27] underscore the critical role of solute elements in steel interacting with irradiation-induced point defects. Granberg et al. [28] demonstrated that irradiation effects vary with different Cr concentrations, with low chromium alloys exhibiting ordered distribution and high chromium alloys showing segregation. Molecular dynamics simulations by Terentyev et al. [6] highlighted that both irradiation dose and Cr concentration significantly affect yield stress, particularly through chromium segregation on dislocation rings enhancing ferrite hardening.

Chen et al. [29] used transmission electron microscopy to study dislocation loop growth under irradiation in alloys with 0.6 wt.% Ni, finding distinct growth behaviors for different types of dislocation loops with respect to irradiation dose. Jia et al. [30] investigated the impact of alloying elements on RPV steel irradiation embrittlement, ranking their influence as Cu > Ni > Mn / Si / P. They identified synergistic effects between Cu-Ni and Mn-Ni using neural network approaches. These findings collectively contribute to a deeper understanding of how solute elements and their interactions with irradiation conditions influence the embrittlement mechanisms in RPV steels, guiding the development of more robust predictive models for material performance in nuclear environments.

The impact of both irradiation dose and solute element content on the macroscopic mechanical properties of materials is crucial and cannot be overlooked. Understanding these relationships requires detailed predictions at the microscale through extensive computational simulations and correlation with microscopic testing methods. However, conducting such studies at the microscopic level remains challenging and less accessible. In this work, we investigate the effects of neutron irradiation on the tensile properties of Fe-0.74wt.%Ni alloy using molecular dynamics simulations with LAMMPS software based on machine-learning interatomic potential, where trained data are generated from first-principles calculations. The simulations explore the synergistic effects of cascade events and defects on the tensile behavior of the alloy by varying three key factors: MD-dpa (displacements per atom due to irradiation), solute element content in the alloy, and temperature. The computational results presented in this paper contribute to the analysis

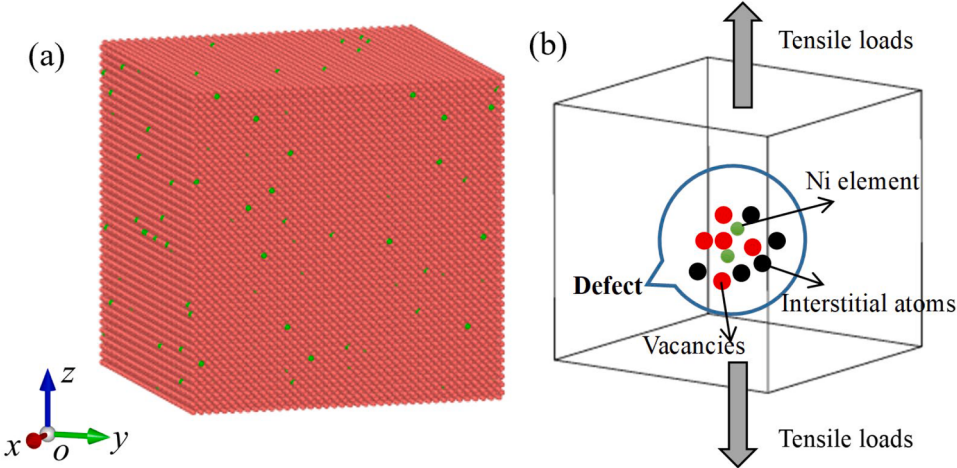


**Fig. 2.** (a) Irradiated structural model of Fe-0.74 wt% Ni alloy and (b) the schematic diagram of uniaxial stretching.

and bridging of data from the microscale to the finer scales in multi-scale simulations, facilitating the development and refinement of models for irradiation hardening and embrittlement, thereby enhancing our understanding of material performance under extreme nuclear environments.

## 2. Calculation models and methods

All simulations in this paper were performed using LAMMPS software [32] based on the molecular dynamics method (MD) [31], using the trained gaussian approximation potential [33] to describe Fe-Ni atomic interactions. The OVITO software [34] was used for the visual analysis of the irradiation and stretching results, and DXA [35] was used for the identification of defects.

Based on density functional theory, first-principles calculations were conducted using the Vienna *ab initio* Simulation Package (VASP) [36,37] to evaluate the total energy of the Fe-Ni structures, where the inequivalent structures are generated by the *Structures of Alloy Generation And Recognition* code [38]. The high-throughput calculation platform was developed to perform automatic calculations and generate a database upon completion for training machine learning interatomic potentials as exemplified in Fig. 1(a). The exchange-correlation functional was treated with the Perdew-Burke-Ernzerhof (PBE) formulation within the generalized gradient approximation (GGA) framework [39]. A kinetic energy cutoff of 400 eV was applied for the plane waves, and the energy convergence criterion was set to  $10^{-5}$  eV. The atomic positions and lattice parameters were fully optimized until the forces on all atoms were  $<0.01$  eV/Å. Since the Fe and Ni are magnetic materials, the spin-polarization calculations were performed to obtain all the properties for Fe-Ni structures.

We created a single-crystal iron (Fe) box with dimensions of  $40a \times 40a \times 40a$ , containing a total of 128,000 atoms. A portion of the iron atoms were selectively replaced with nickel (Ni) atoms to construct Fe-Ni alloy structures with varying concentrations. And the Fe-Ni system utilized three-dimensional periodic boundary conditions. In order to simulate the dynamic evolution following irradiation, the system was fully relaxed in an *NPT* (isothermal-isobaric) ensemble for 20 ps, with the central atom of the box chosen as the primary knock-on atom (PKA) with a randomly oriented velocity. Evolution over 20 ps was carried out using variable time steps under the *NVE* (constant energy) ensemble with atomic rate-limiting techniques. During this process, we monitored the nature of defects, including interstitials and vacancies, at various time intervals. Once the system reached ensemble equilibrium, we began calculating the stress-strain curve to simulate the mechanical properties of the system under specified temperatures and Ni

concentrations.

## 3. Results and discussions

### 3.1. High-throughput calculations and GAP model construction

For the Fe-Ni alloy structure, various atomic compositions and distributions should be considered to maintain the structural diversity of candidates for the proceeding machine learning potential training. We take a unit cell of 16 atoms for bcc Fe as the prototype structure to enumerate all possible Fe-Ni alloy configurations. The formation energy is defined by  $E_f = E[\text{Fe}_x\text{Ni}_{(1-x)}] - xE[\text{Fe}] - (1-x)E[\text{Ni}]$ , where  $E[\text{Fe}_x\text{Ni}_{(1-x)}]$  is the energy of Fe-Ni alloy configuration,  $E[\text{Fe}]$  and  $E[\text{Ni}]$  are the average energies of bcc Fe and Ni structure, respectively. The formation energies are found to be negative at some certain concentrations, indicating that Fe-Ni alloy is the ordered substitutional solid solution with approximately 25% Fe concentration as shown in Fig. 1(b). Note that the ground state structure is  $\text{FeNi}_3$  structure as shown in the left lower corner of Fig. 1(b), in which all Fe atoms are surrounded by Ni atoms, demonstrating that the uniform distribution of Fe and Ni can effectively enhance the stability of the system. When Fe and Ni atoms aggregate separately, grain boundaries are formed, leading to an increase in energy and a decrease in the stability.

Based on these inequivalent Fe-Ni configurations, we employ the gaussian approximation potential (GAP) model to interpolating interatomic potential energy surfaces of Fe-Ni system, using the smooth overlap of atomic positions (SOAP) kernel. The total GAP energy for Fe-Ni system is defined by a sum of the two-body and three-body potential and the many-body SOAP kernel:

$$E = \sum_{i < j} V^{(2)}(\mathbf{r}_{ij}) + \sum_{i < j < k} V^{(3)}(\mathbf{r}_{ij}, \mathbf{r}_{ik}, \mathbf{r}_{jk}) + \sum_i \sum_s^M \alpha_s K(\mathbf{R}_i, \mathbf{R}_s)$$

where  $i$  and  $j$  represent the indices of the atoms within the Fe-Ni structures. The term  $V^{(2)}$  denotes the two-body pair potential, while  $V^{(3)}$  signifies the three-body pair potential.  $K$  is the basis function of the SOAP kernel, and  $\mathbf{R}_i$  represents the collection of relative position vectors corresponding to the neighbors of atom  $i$ .

The initial training set included about 200 Fe-Ni alloy structures, where two-body and three body interaction are considered to fit the GAP model. The fitting consistency result is shown in Fig. 1(c), the total energy predicted by GAP model has excellent agreement with the DFT results, in which the mean absolute error is 2.62 meV/atom. For the performance metric of our trained model is detailed in the support information.

**Table 1**

Parameter setting for the cascade collision process.

Simulation projects	Cascade effect
Box size	$40a \times 40a \times 40a$
Potential functions	GAP model
Number of atoms	128,000
Fe-Ni alloy lattice constants ( $\text{\AA}$ )	$a = 2.9189$
Time steps (ps)	0.001
Simulated temperature (K)	573
Ni element content (wt%)	Fe-0.74%Ni
PKA energy (keV)	1,2,3,4,5
MD-dpa	$7.8125 \times 10^{-5}, 1.5625 \times 10^{-4}, 2.3438 \times 10^{-4}, 3.125 \times 10^{-4}, 3.906 \times 10^{-4}$

**Table 2**

Parameter setting for stretching process.

Simulation projects	Uniaxial stretching
Read irradiation output files	Last step(20 ps)
Potential functions	GAP model
strain rate	$5 \times 10^9 \text{ s}^{-1}$
Time steps (ps)	0.001
Simulated temperature (K)	300,500,700,900 and 1100
Ni element content (wt%)	0%,0.74%,1%,5%,10%,20%

To train a robust GAP model iteratively, we continued to generate larger Fe-Ni structures to enhance the training database. As a result, the fitting error finally converged to 2.62 meV/atom, as shown in Fig. 1(d). The prediction error for the test dataset was 2.85 meV/atom, indicating that the trained GAP model can accurately describe the Fe-Ni system. Additionally, to perform large-scale molecular dynamic simulations, we generated Fe-Ni structures consisting of 1024 atoms to compare the total energy predicted by the GAP model and DFT. The mean absolute error for these predictions is 3.15 meV/atom, demonstrating the accuracy of

our trained model. Therefore, the trained GAP model was suitable for performing molecular dynamics simulations on large Fe-Ni systems. The specific simulation process is carried out in two steps as follows, and the simulation schematic diagram is shown in Fig. 2.

### 3.2. Cascade effect

#### 3.2.1. Cascade collision process simulation

A box of single crystal Fe with dimensions of  $40a \times 40a \times 40a$  was created for the simulation. The x, y, and z coordinates were aligned along the [100], [010], and [001] directions, respectively, resulting in a total of 128,000 atoms in the box. Some of the Fe atoms were replaced by Ni atoms. To avoid edge effects, the system utilized three-dimensional periodic boundary conditions. The time step was set to 0.001 ps, and the temperature considered was the actual operating temperature of 573 K at the location of the nuclear power reactor pressure vessel (RPV) steel. The simulated system required full relaxation (20 ps) in the NPT (isothermal-isobaric) environment, with the central atom of the selected box being a primary knock-on atom (PKA)

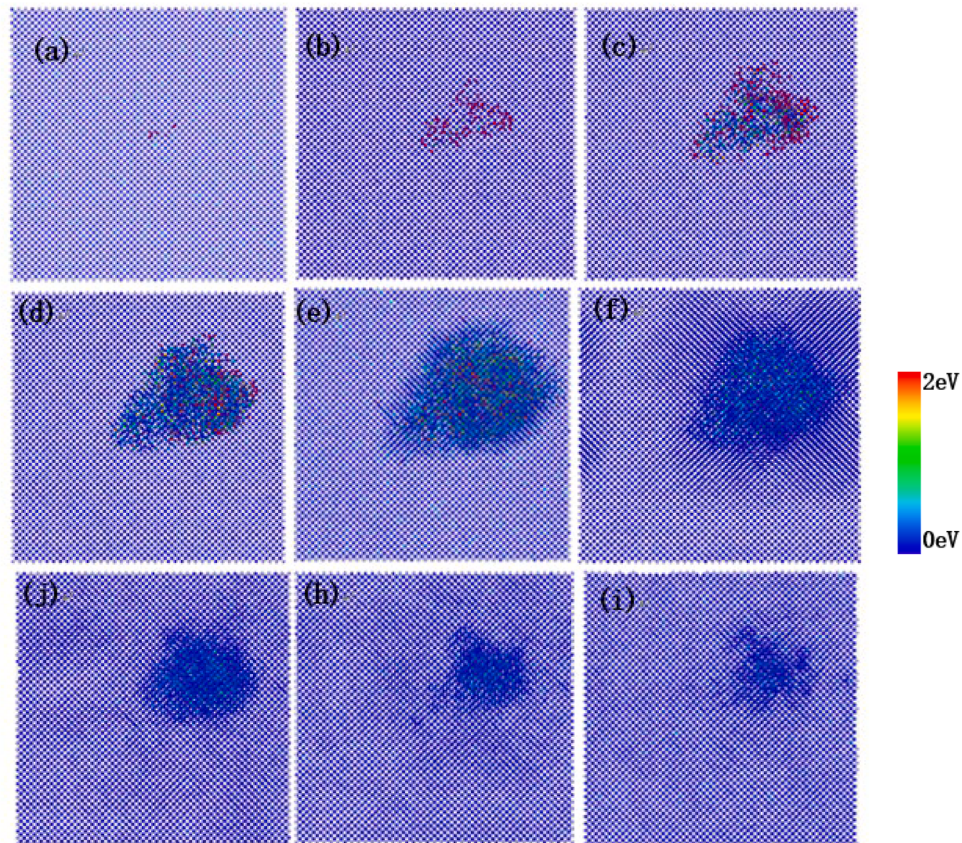


**Fig. 3.** Evolution of the atoms in the shift cascade with cascade time at energy of 5 keV. (a:0.01 ps; b:0.05 ps; c:0.1 ps; d:0.5 ps; e:1 ps; f:1.5 ps; j:2.5 ps; h:3 ps; i:5 ps).

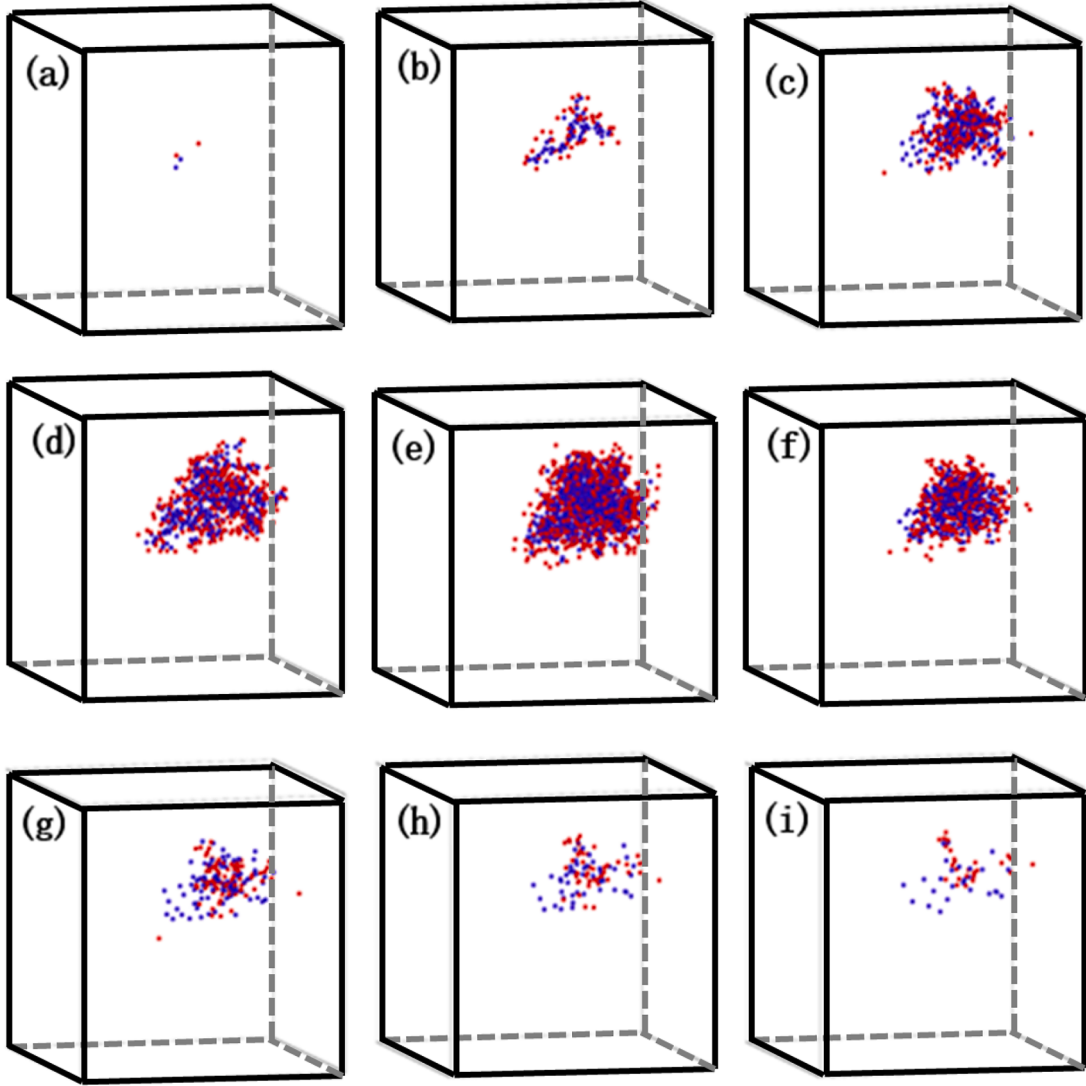


**Fig. 4.** Evolution of point defects in the shift cascade with cascade time at energy of 5 keV (a:0.01 ps; b:0.05 ps; c:0.1 ps; d:0.5 ps; e:1 ps; f:1.5 ps; g:2.5 ps; h:3 ps; i:5 ps), (red for interstitial atoms, blue for vacancies).

oriented randomly. Evolution over 20 ps with variable time steps was carried out under the NVE (constant energy) ensemble using atomic rate-limiting techniques. The relationship between energy and PKA velocity is given by  $E = mv^2/2$ . To account for statistical error in the calculations, each simulation was repeated 20 times and the average value was taken. The relevant parameters considered in the model are shown in Table 1. Furthermore, we have added the evidence for choosing the PKA energy and simulation temperature in the Support information.

### 3.2.2. Uniaxial stretching process simulation

For the uniaxial stretching process simulation, the results file from the irradiation simulation was used as input. The same potential function and periodic boundary conditions were applied as in the irradiation simulation. Energy minimization of the irradiation simulation results file was achieved using the conjugate gradient method, followed by full relaxation of the minimized structural model using *NPT* ensemble to bring the structure to its most stable state. Temperature control via the Nose-Hoover method ensured that the simulated system reached equilibrium at the specified temperature before loading. The model was then stretched along the y-axis using the deform command with a strain rate of  $5 \times 10^9/\text{s}$ . The *NVT* ensemble was used for the stretching process, and the relevant parameters were set as shown in Table 2. We have added the

evidence for choosing the Ni element content in the Support information.

The evolution of atomic and point defects in the shift cascade with cascade time at an energy of 5 keV are shown in Figs. 3 and 4, respectively. The PKA atom, initially given a velocity, collides with neighboring atoms, producing primary recoil atoms. These recoil atoms then collide with their neighbors, continuing a series of collisions until the process concludes.

Figs. 3 and 4(a)~(c) depict the collision stage, where initial energy transfer causes some atoms in the lattice to move, creating a highly disordered region that grows rapidly. Figs. 3 and 4(d)~(f) illustrate the thermal peak stage, during which atoms in a localized region with high deposition energy density share collision energy, forming a melting zone. Collisions among secondary recoil atoms convert kinetic energy into thermal energy, raising the local temperature and resulting in a collective effect. Figs. 3 and 4(g)~(i) represent the quenching stage, where the molten zone solidifies, defects diffuse rapidly, most atoms return to their perfect lattice positions, and non-thermal recombination processes occur, leaving only a few defects. At this stage, vacant defects mainly occupy the center of the defective site, while interstitial defects are primarily located at the periphery and are more densely packed than the surrounding interstitial atoms. Figs. 3 and 4(j)~(l) show the

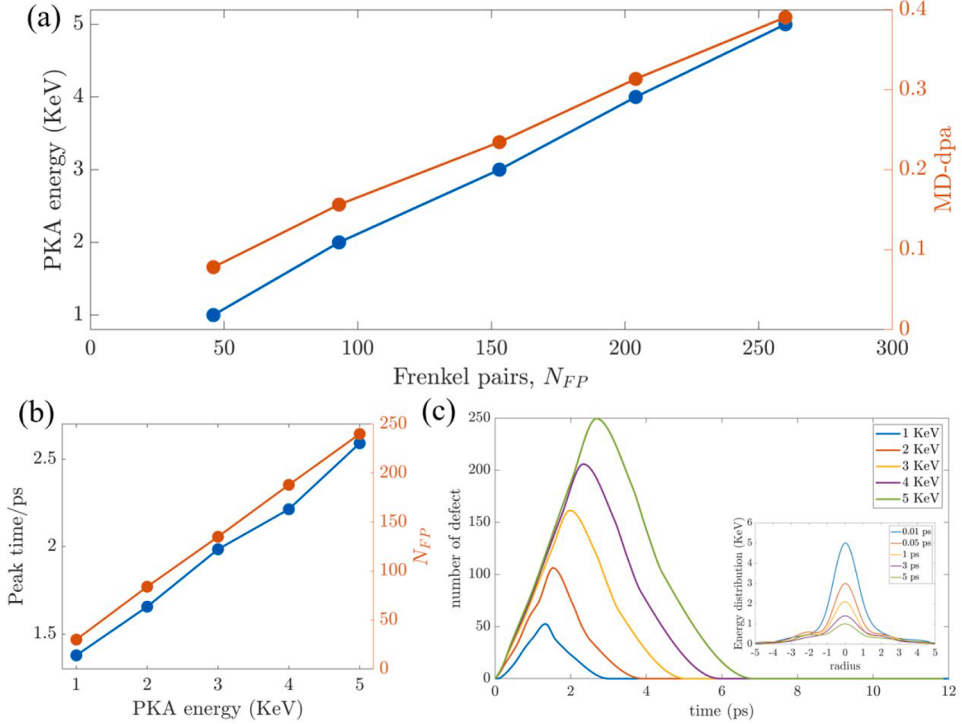


**Fig. 5.** (a) relationship of Frenkel Pairs peak with PKA energy and MD-dpa. Under different PKA energy, (b) relationship of Frenkel Pairs with cascade time; (c) relationship of time and number of defects peaking with PKA energy.

composite stage, where defects spread slowly and form clusters. The temperature stabilizes, resulting in a primary damage state consisting of point defects and their clusters. A complete cascade collision process includes four stages: defect creation, dislocation peak appearance, defect annihilation, and cascade annealing, leading to the formation of stable defects.

In the evolution of point defects in Fe-Ni alloy, the dislocations undergo a change in their configuration, resulting in the formation of dislocation loops or rings. This transformation is typically observed in materials under irradiation or high stress. Dislocations, which are line defects in the crystal structure that facilitate plastic deformation, can interact with other defects, such as vacancies or interstitial atoms (created by irradiation or stress). When enough energy is introduced into the system, these interactions can cause the dislocation lines to close and form loops or rings. This process is particularly common in irradiated materials, where defect clusters (like voids or interstitial clusters) act as pinning points that cause dislocations to bow and eventually close into loops. The formation of dislocation rings instead of lines has significant implications for the material's mechanical properties. Dislocation loops can hinder the movement of other dislocations, increasing the material's strength (a phenomenon known as radiation hardening), but at the same time, they can reduce ductility, making the material more prone to embrittlement under stress. This transformation from lines to loops is an essential aspect of understanding material behavior under extreme conditions, especially in nuclear or high-stress environments.

### 3.3. Effect of MD-dpa on irradiation defects

In this work, the NRT model [36] is employed to predict the number of atoms ( $N_d$ ) that become delocalized in Fe-0.74 wt.% Ni alloy after PKA atomic collisions, enabling the calculation of the delocalization probability MD-dpa, as shown by the equations:

$$N_d = 0.8E_D/2E_d \quad (1)$$

$$DPA = N_d/n_0 \quad (2)$$

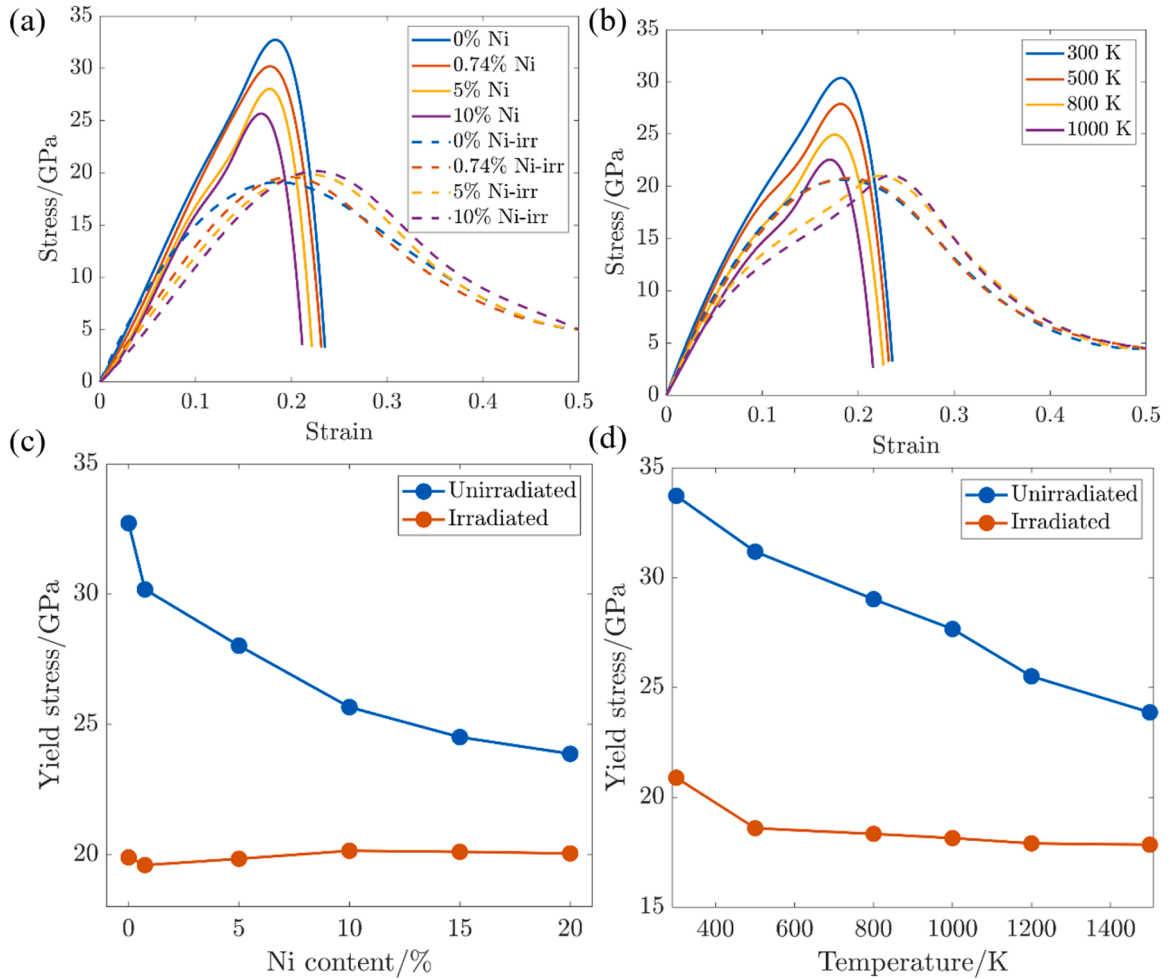
According to the ASTM standard [37],  $E_d$  for Fe is 0.04 keV, where  $n_0$  represents the number of atoms per unit volume of the material, and  $E_D$  denotes the energy of the initial delocalized atom causing delocalization.

Fig. 5(a) depicts the relationship between the peak number of Frenkel pairs defects and PKA energy, as well as MD-dpa after irradiation simulation. The darker regions in the five small plots indicate disordered areas where atoms are delocalized at corresponding PKA energies. PKA energy correlates proportionally with MD damage dose without changing the size of the simulated box. As  $N_{FP}$  increases with rising MD-dpa, higher PKA energies lead to more intense collisions with neighboring atoms, thereby increasing the number of recoil atoms and subsequently elevating the number of delocalized atoms.

In Fig. 5(b) and (c), the evolution of Frenkel pairs defects in relation to PKA is further detailed. The cascade process progresses through four stages: collision, thermal peak, compound, and stabilization, which align with the cascade evolution illustrated in Figs. 2 and 3. As shown in the inset of Fig. 4(c), we focus on the state when PKA is 5 KeV, where the energy diffused from the center to neighboring rapidly due to the cascade effect. The energy was initially Gaussian distribution, and would evaluate to a uniform distribution after enough atomic collision. The peak in Frenkel defect pairs increases with higher PKA energy, and the time taken to reach this peak extends, indicating a prolonged thermal peak phase. This extension is attributed to enhanced energy transfer among atoms due to higher initial colliding atom energies, facilitating sustained collisions that generate more recoil atoms and delocalized atoms over an extended duration.

### 3.4. Synergistic effect of Ni content and irradiation defects on tensile properties

The tensile stress-strain curves for unirradiated and irradiated conditions are systematically investigated under the ML-based MD simulations. Unirradiated tensile stress decreases gradually (Fig. 6(a)), and



**Fig. 6.** (a) The unirradiated and irradiated stress-strain curve under different Ni content. (b) The unirradiated and irradiated stress-strain curve under different temperature for Fe-0.74 wt% Ni alloy. (c) The unirradiated and irradiated yield stress curve under different Ni content. (d) The unirradiated and irradiated yield stress curve under different temperature for Fe-0.74 wt% Ni alloy.

strain at yield reduces with Ni content increases (Fig. 6(b)), suggesting Ni diffusion occurs via a vacancy mechanism during plastic deformation. This diffusion, combined with the aggregation of vacancies and irradiation defects, leads to the formation of holes and dislocations, causing material embrittlement. After irradiation, the stress-strain curve

indicates lower stress compared to unirradiated conditions. This is attributed to dislocation formation between irradiation-induced point defects and solute Ni elements under tensile stress.

Ni diffusion via a vacancy mechanism accelerates hole formation, easing plastic deformation and reducing required stress. For the higher

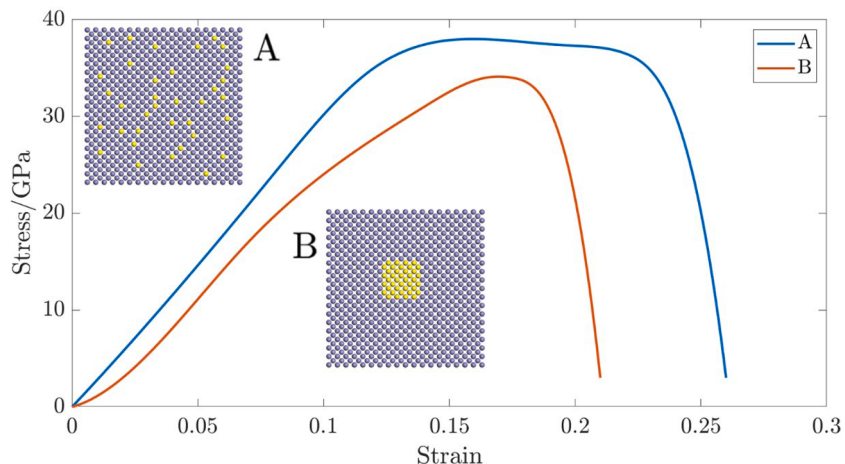


**Fig. 7.** The stress-strain curve for different distribution of Ni atoms, where A is the uniform distribution and B is the phase-separated distribution. The Fe-Ni alloy structures are plotted in the inset, where the yellow atoms denote Ni atoms and brown atoms denote Fe atoms.

temperature, the atomic movement will be dramatically faster, and the crystal structure will be more unstable, which induces that the stress will be lower under the same strain when the temperature becomes larger. As shown in Fig. 6(b), the stress peak decreases with the increase of temperature for both unirradiated and irradiated cases, suggesting that the high temperature will destroy the Fe-Ni alloy structure more rapidly.

Note that the Yield stress is a planitia under the irradiated case compared with the unirradiated case as shown in Fig. 6(c) and (d), which attributes to the distribution of Ni atoms. After irradiation, Ni atoms diffuse extensively in the Fe-Ni alloy, achieving a uniform distribution. This diffusion provides a cushioning effect during tensile deformation, preventing fracture that would otherwise occur more easily at the Fe-Ni grain boundaries.

To address this issue, we constructed two representative FeNi alloy structures: in alloy A, Ni atoms are uniformly distributed, while in alloy B, Ni atoms are segregated at grain boundaries in bcc-Fe as shown in the inset of Fig. 7. These two structures represent the phase-separated distribution of Fe-Ni before irradiation and the uniform distribution after irradiation, respectively. As shown in Fig. 7, the stress-strain curve of alloy A provides a cushioning effect during tensile deformation, resulting in a more gradual slope before fracture. For the alloy B, when the stress reaches the yield stress, the alloy will rapidly fracture due to the Ni grain boundary, indicating that the Ni distribution will effectively influences the behavior of the stress-strain curve. The uniformly distributed Ni atoms will effectively enhance the cushioning between Fe and Ni atoms during tensile deformation, thereby improving the mechanical properties of the Fe-Ni alloy and enabling it to withstand higher tensile strain.

#### 4. Conclusion

The neutron irradiation of Fe-0.74 wt% Ni alloys was systematically investigated based on high-throughput density functional theory calculations and molecular dynamics simulations combined with GAP model, and the following conclusions can be drawn. The results can provide data to support the linking of micro scale to fine scale ties and the optimization of relevant irradiation models.

- (1) Cascade Process: The irradiation induces a cascade effect comprising four stages: collision, thermal peak, compounding, and stabilization. There is a linear increase in Frenkel Pairs defects with MD-dpa and PKA energy.
- (2) Defect Interaction and Tensile Properties: Post-irradiation, residual point defects and Ni vacancy diffusion create holes and dislocations. Increasing strain reduces voids and transforms dislocation lines into rings, lowering tensile stress compared to unirradiated material.
- (3) Temperature Effects: Temperature influences defect evolution and the strength of dislocation-defect interactions, modifying defect density. Higher temperatures enhance dislocation annihilation and decrease the defect hardening coefficient, leading to lower macroscopic flow stress.
- (4) Uniform distribution of Ni atoms: The uniformly distributed Ni atoms can act as a buffer during the tensile deformation of the Fe-Ni alloy, resulting in superior localized mechanical properties, while the aggregated Ni atoms will serve as the grain boundary and make Fe-Ni alloy more prone to fracture.

#### CRediT authorship contribution statement

**Chang-Chun He:** Writing – review & editing, Writing – original draft, Software, Methodology. **Fen Ren:** Methodology, Investigation, Data curation, Conceptualization. **Xiao-Bao Yang:** Writing – review & editing, Supervision, Conceptualization. **Guixi Wu:** Writing – review & editing, Conceptualization. **Shuyan Zhang:** Writing – review & editing, Conceptualization.

#### Declaration of competing interest

The authors declare that they have no known competing financial interests or personal relationships that could have appeared to influence the work reported in this paper.

#### Acknowledgements

The authors are grateful for the supports provided by the Major Program of Basic and Application-oriented Basic Research Foundation of Guangdong Province (Project No. 2019B030302011). Guangdong Innovative and Entrepreneurial Research Team Program (Project No. 2016ZT06G025). Guangdong Provincial Key Laboratory of Functional and Intelligent Hybrid Materials and Devices (Grant No. 2023-GDKLFIHMD-04). the Guangdong Basic and Applied Basic Research Foundation (Grant No. 2023A1515110894).

#### Supplementary materials

Supplementary material associated with this article can be found, in the online version, at [doi:10.1016/j.physleta.2024.129992](https://doi.org/10.1016/j.physleta.2024.129992).

#### Data availability

Data will be made available on request.

#### References

- [1] D.J. Naus, C.B. Oland, B.R. Ellingwood, H.L. Graves, W.E. Norris, Aging management of containment structures in nuclear power plants, *Nucl. Eng. Des.* 166 (1996) 367–379.
- [2] D.J. Naus, Primer On Durability of Nuclear Power Plant Reinforced Concrete Structures – A review of Pertinent factors, NUREG/CR-6927 (ORNL/TM-2006/529), Oak Ridge National Laboratory, Oak Ridge, Tennessee, February 2007.
- [3] T. Allen, J. Busby, M. Meyer, D. Pettit, Materials challenges for nuclear systems, *Mater. Today*. 13 (2010) 14–23.
- [4] S.J. Zinkle, G.S. Was, Materials challenges in nuclear energy, *Acta Mater* 61 (2013) 735–758.
- [5] Y. Li, W. Xiao, H. Li, Molecular dynamics simulation of C/Si ratio effect on the irradiation swelling of  $\beta$ -SiC, *J. Nucl. Mater.* 480 (2016) 75–79.
- [6] D.J. Edwards, B.N. Singh, J.B. Bilde-Sørensen, Initiation and propagation of cleared channels in neutron-irradiated pure copper and a precipitation hardened CuCrZr alloy, *J. Nucl. Mater.* 342 (2005) 164–178.
- [7] D. Terentyev, F. Bergner, Y. Ossetsky, Cr segregation on dislocation loops enhances hardening in ferritic Fe-Cr alloys, *Acta Mater* 61 (2013) 1444–1453.
- [8] G.R. Odette, T. Yamamoto, T.J. Williams, R.K. Nanstad, C.A. English, On the history and status of reactor pressure vessel steel ductile to brittle transition temperature shift prediction models, *J. Nucl. Mater.* 526 (2019) 151863.
- [9] Integrity of Reactor Pressure Vessels in Nuclear Power Plants:Assessment of Irradiation Embrittlement Effects in Reactor Pressure Vessel steels, Report No NP-T-3.11, International Atomic Energy Agency, Vienna, 2009.
- [10] R.K. Nanstad, G.R. Odette, M.A. Sokolov, in: Proceedings of the ASME pressure vessels and piping conference, 2010, p. 125, 9.
- [11] M. Nastar, F. Soisson, Radiation-Induced Segregation. *Compr. Nucl. Mater.*, Elsevier, 2012, pp. 471–496.
- [12] S.J. Zinkle, Radiation-Induced Effects on Microstructure. *Compr. Nucl. Mater.*, Elsevier, 2020, pp. 91–129.
- [13] Y.N. Ossetsky\*, R.E. Stoller, Atomic-scale mechanisms of helium bubble hardening in iron, *J. Nucl. Mater.* 465 (2015) 448–454.
- [14] K. Ono, M. Miyamoto, K. Arakawa, R.C. Birtcher, Dynamical response of helium bubble motion to irradiation with high-energy self-ions in aluminum at high temperature, *Philos. Mag.* 89 (2009) 513–524.
- [15] Y.N. Ossetsky, D.J. Bacon, Atomic-Level Dislocation Dynamics in Irradiated Metals, *Compr. Nucl. Mater.* (2012) 333–356. Elsevier.
- [16] K. Nordlund, Historical review of computer simulation of radiation effects in materials, *J. Nucl. Mater.* 520 (2019) 273–295.
- [17] K. Lai, K.G. Li, H.H. Wen, Synergistic effects of applied strain and cascade overlap on irradiation damage in BCC iron, *J. Nucl. Mater.* 542 (2020) 152422.
- [18] S.M. Zamzamian, S.A. Hossein Feghhi, M. Samadfar, A study on the mobility of  $1/2<111>\{011\}$  edge dislocation in low-carbon  $\alpha$ -Fe and its interactions with damage cascade: on picosecond time scale using molecular dynamics simulations, *J. Nucl. Mater.* 527 (2019) 151806.
- [19] Y.N. Ossetsky, G.M. Pharr, J.R. Morris, Two modes of screw dislocation glide in fcc single-phase concentrated alloys, *Acta Mater* 164 (2019) 741–748.
- [20] X. Wang, N. Gao, Y. Wang, H. Liu, G. Shu, C. Li, B. Xu, W. Liu, Molecular dynamics study on the Burgers vector transition of nanometric dislocation loops induced by cascade in bcc-iron, *J. Nucl. Mater.* 519 (2019) 322–331.

- [21] Q. Peng, F. Meng, Y. Yang, C. Lu, H. Deng, L. Wang, S. De, F. Gao, Shockwave generates <100>dislocation loops in bcc iron, *Nat. Commun.* 9 (2018) 4880.
- [22] X. Wang, N. Gao, Y. Wang, X. Wu, G. Shu, C. Li, Q. Li, B. Xu, W. Liu, Formation of <100>dislocation loop in bcc-Fe via the ternary loop reaction, *Scr. Mater.* 162 (2019) 204–208.
- [23] F.J. Pérez-Pérez, R. Smith, Structural changes at grain boundaries in bcc iron induced by atomic collisions, *Nucl. Instrum. Methods Phys. Res. Sect. B Beam Interact. Mater. At.* 164–165 (2000) 487–494.
- [24] A. Bakaev, D. Terentyev, X. He, D. Van Neck, Synergetic effects of Mn and Si in the interaction with point defects in bcc Fe, *J. Nucl. Mater.* 455 (2014) 5–9.
- [25] P. Olsson, C. Domain, J. Wallenius, Ab initio study of Cr interactions with point defects in bcc Fe, *Phys Rev B* 75 (1) (2007).
- [26] E. Vincent, C.S. Becquart, C. Domain, Ab initio calculations of vacancy interactions with solute atoms in bcc Fe, *Nucl. Instrum. Methods Phys. Res. Sect. B Beam Interact. Mater. At.* 228 (2005) 137–141.
- [27] E. Vincent, C.S. Becquart, C. Domain, Ab initio calculations of self-interstitial interaction and migration with solute atoms in bcc Fe, *J. Nucl. Mater.* 359 (2006) 227–237.
- [28] F. Granberg, J. Byggmästar, K. Nordlund, Defect accumulation and evolution during prolonged irradiation of Fe and FeCr alloys, *J. Nucl. Mater.* 528 (2020) 151843.
- [29] L. Chen, K. Murakami, D. Chen, H. Abe, Z. Li, N. Sekimura, In situ transmission electron microscopy study of growth of dislocation loops in Fe-Ni alloy under ion irradiation, *Scr. Mater.* 187 (2020) 453–457.
- [30] L.X. Jia, H. Xu, B. Bing, Study of the effect of alloying elements on the irradiation embrittlement of reactor pressure vessel steel using a neural network approach, *Atom. Scien. & Tech.* 54 (2020) 2174–2181 (in Chinese).
- [31] W. Cai, J. Li, B.P. Uberuaga, S. Yip, *Molecular Dynamics. Compr. Nucl. Mater.*, Elsevier, 2020, pp. 573–594.
- [32] S. Plimpton, Fast parallel algorithms for short-range molecular dynamics, *J. Compu. Phys.* 117 (1995) 1–19.
- [33] Albert P. Bartók, Mike C. Payne, Risi Kondor, Gábor Csányi, Gaussian Approximation Potentials: the Accuracy of Quantum Mechanics, without the Electrons, *Phys. Rev. Lett.* 104 (2010) 136403.
- [34] A. Stukowski, Visualization and analysis of atomistic simulation data with OVITO—the Open Visualization Tool, *Model. Simul. Mater. Sci. Eng.* 18 (2010) 015012.
- [35] A. Stukowski, V.V. Bulatov, A. Arsenlis, Automated identification and indexing of dislocations in crystal interfaces, *Model. Simul. Mater. Sci. Eng.* 20 (2012) 085007.
- [36] G. Kresse, J. Furthmüller, *Phys. Rev. B* 54 (1996) 11169–11186.
- [37] G. Kresse, J. Furthmüller, *Comput. Mater. Sci.* 6 (1996) 15–50.
- [38] Chang-Chun He, Ji-Hai Liao, Shao-Bin Qiu, Yu-Jun Zhao, Xiao-Bao Yang, *Comput. Mater. Sci.* 193 (2021) 110386.
- [39] W. Kohn, L.J. Sham, *Phys. Rev.* 140 (1965) A1133–A1138.